PNAS RESEARCH ARTICLE | BIOPHYSICS AND COMPUTATIONAL BIOLOGY

Molecular mechanism of Arp2/3 complex activation by nucleation-promoting factors and an actin monomer

Sahithya Sridharan Iyer[a], Jiangbo Wu[a], Thomas D. Pollard[b,c,d,1,2], and Gregory A. Voth[a,1]

Affiliations are included on p. 10.

Edited by Brad J. Nolen, University of Oregon, Eugene, OR; received October 17, 2024; accepted January 23, 2025 by Editorial Board Member J. A. McCammon

Arp (actin-related protein) 2/3 complex nucleates actin filament branches on the sides of preexisting actin filaments during cell and organelle movements. We used computer simulations of mammalian Arp2/3 complex to address fundamental questions about the mechanism. Metadynamics and umbrella free energy sampling simulations of the pathway revealed that a clash between the D-loop of Arp2 and Arp3 produces an energy barrier of 20 ± 6 kcal/mol between the inactive splayed and active short-pitch conformations of Arp2/3 complex. Atomistic molecular dynamics simulations showed that binding the CA motif of the nucleation-promoting factor Neuronal Wiskott-Aldrich Syndrome Protein (N-WASp) to inactive, splayed Arp2/3 complex shifts it toward the short-pitch active conformation and opens a binding site for an actin monomer on Arp3. Other simulations showed that this actin monomer stabilizes a transition state of Arp2/3 complex. These observations together with prior experimental work provide insights required to propose a physically grounded pathway for actin filament branch formation.

Arp2/3 complex | actin filament branching | nucleation-promoting factor | molecular dynamics

Significance

Arp (actin-related protein) 2/3 complex, a large protein with seven subunits, assembles branched actin filaments, which generate forces for cell and organelle movements. Arp2/3 complex is natively inactive and must undergo large conformational changes to transition into the active state in the branch junction. Proteins called nucleation-promoting factors and actin filaments assist in branch formation but their mechanisms are incompletely characterized. Our molecular dynamics simulations of several cryo-electron microscopy (cryo-EM) structures of Arp2/3 complex revealed energy barriers and kinetic and thermodynamic parameters of actin filament branch formation. We used these insights to propose a biophysically supported pathway for branch formation.

Arp (actin-related protein) 2/3 complex (Fig. 1) is an important actin binding protein that regulates actin filament assembly. The complex produces actin filaments for cellular and organelle movements by nucleating filaments (1) that grow as branches at a 70° angle from the sides of existing filaments (2). Arp2/3 complex consists of seven-subunits including two actin-related proteins, Arp2 and Arp3, a seven-blade β-propeller subunit ARPC1, and four structurally unique subunits ARPC2-5 that support the Arps (Fig. 1) (3–7). In the branch junction, the Arps are positioned next to each other like two subunits along the short pitch helix of an actin filament, so they can serve as the first two subunits in the daughter filament (8–12).

Native Arp2/3 complex from animals and fission yeast is inactive (Fig. 1*A*), since the scaffolding subunits hold Arp2 and Arp3 apart in a splayed conformation. Thus, a massive conformational change is required to rotate the Arps next to each other (Fig. 1*B*) so they can serve as the base of the branch filament, anchoring the pointed end of the growing daughter filament (Fig. 1*C*).

Arp2/3 complex requires help from proteins called nucleation-promoting factors (NPFs) to nucleate a new filament. The DIP1 family of NPFs can activate Arp2/3 complex to nucleate an unbranched filament on their own (13). NFPs related to the Wiskott–Aldrich syndrome protein, WASp, cooperate with actin filaments to form branches. WASp-family NPFs have a verprolin (V) motif that binds an actin monomer and a central and acidic (CA) motif (i.e., VCA) that binds Arp2/3 complex (14–16). Actin-VCA bound to Arp2/3 complex moves the Arps closer together (17) and favors binding to actin filaments (18) and nucleation of a new filament that grows as a branch from the mother filament (19). However, this process is unfavorable, since Arp2/3 complex with bound VCA-actin binds only transiently to the side of an actin filament, and few of these interactions produce a branch (20). In contrast, budding yeast Arp2/3 complex has some spontaneous nucleation activity on its own (21).

Thus, the key question for the past 25 y has been, how do WASp-type NPFs and actin filaments work together to produce actin filament branches (22, 23)? Structural, biochemical, and computational studies have generated extensive, detailed information about the process, but many unresolved issues remain. For example, a cryo-EM reconstruction of Arp2/3 complex with two copies of N-WASp-CA has the conformation of the inactive state (24). On the other hand, NPF binding promotes chemical crosslinking between cysteines engineered into Arp2 and Arp3, which is only possible in the short-pitch, active conformation (21, 25). Another question is why formation of a branch from Arp2/3 complex with VCA on the side of an actin filament is so unfavorable.

Author contributions: S.S.I., J.W., T.D.P., and G.A.V. designed research; performed research; analyzed data; and wrote the paper.

The authors declare no competing interest.

This article is a PNAS Direct Submission. B.J.N. is a guest editor invited by the Editorial Board.

[1]To whom correspondence may be addressed. Email: thomas.pollard@yale.edu or gavoth@uchicago.edu.

[2]Present address: Department of Cell and Molecular Biology, University of California, Berkeley, CA 94720-3202.

This article contains supporting information online at https://www.pnas.org/lookup/suppl/doi:10.1073/pnas.2421467122/-/DCSupplemental.

Published March 6, 2025.

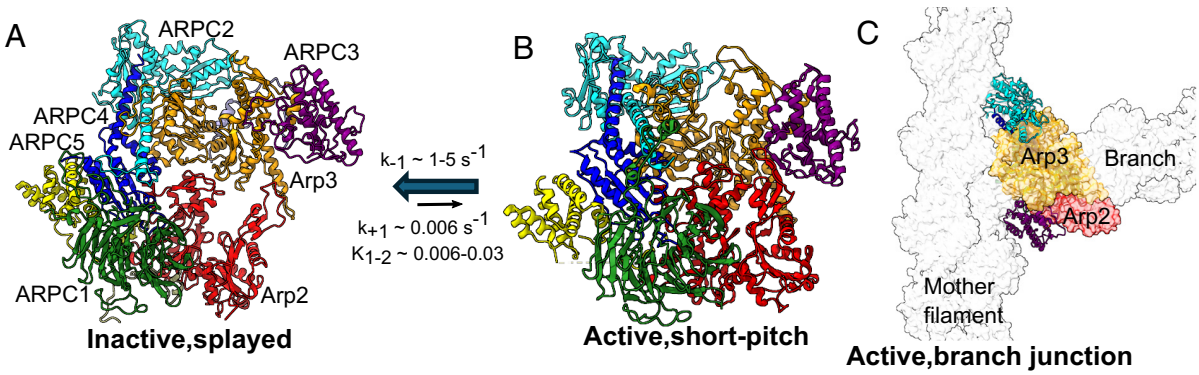

Fig. 1. Overview of structures of Arp2/3 complex. (*A* and *B*) Ribbon diagrams. (*A*) Inactive conformation with the Arp2 and Arp3 subunits held apart in a "splayed" conformation (pdb id: 6UHC). (*B*) Active state from the branch junction. Arp2 and Arp3 are half overlapped like two subunits along the short-pitch helix of an actin filament (pdb id: 7TPT). $K_{1\text{-}2}$ is the equilibrium constant for the transition between these two states, while k_{+1} and k_{-1} are the rate constants for the two reactions. (*C*) Space-filling model of the branch junction with Arp2/3 complex in the short-pitch conformation on the side of the "mother" filament (pdb id: 7TPT).

To understand these apparently conflicting observations and to characterize the structural mechanism of Arp2/3 complex activation, we performed extensive molecular dynamics (MD) simulations at physiological temperature starting with three cryo-EM structures. We used a combination of enhanced free energy sampling via metadynamics and umbrella sampling (26–28) simulations driven by a path collective variable, and unbiased sampling from long equilibrium MD simulations to map the pathway of Arp2/3 complex activation and calculate the energy barriers along the way. These simulations revealed that 1) the inactive and active conformations of Arp2/3 complex are two distinct free energy minima separated by free energy barriers of 20 ± 6 kcal/mol (mean ± SD) and 6 ± 0.7 kcal/mol (mean ± SD) along the pathway of branch formation; 2) two CA motifs bound to Arp2/3 complex shift inactive Arp2/3 complex toward a partially active state and open a binding site for an actin monomer; 3) a single actin monomer bound to Arp3 stabilizes Arp2/3 complex in a transition state; and 4) Arp2/3 complex rapidly reverts back to the inactive conformation after removing the actin monomer from the transition state. This information clarifies how NPFs and actin monomers interact with Arp2/3 complex during the formation of an actin filament branch.

Results

Arp2/3 Complex Crosses a Free Energy Barrier of ~20 kcal/mol between the Inactive and Active States. Activation of Arp2/3 complex involves energetically unfavorable transitions between two stable states, the inactive splayed conformation and active short-pitch conformation found in the branch junction (Fig. 1). A 1 μs equilibrium MD simulation of the active state by Singh et al. (29) and our 3.2 μs simulation of inactive Arp2/3 complex did not have any transitions toward the other state (*SI Appendix*, Fig. S1 and section 1).

We therefore calculated the free energy along the activation pathway of Arp2/3 complex using a combination of metadynamics and umbrella sampling simulations driven by a path collective variable (30, 31) (CV) (Fig. 2). The phrase "collective variable" is often used in metadynamics simulations to denote a "reaction coordinate" or "pathway." Lacking intermediate structures from prior studies, we made an initial estimate of the path of the conformational change with a linear morph between the positions of the backbone atoms in the two states using cryo-EM structures of mammalian Arp2/3 complex in the inactive splayed conformation (pdb id: 6UHC) and the branch junction (pdb id: 7TPT).

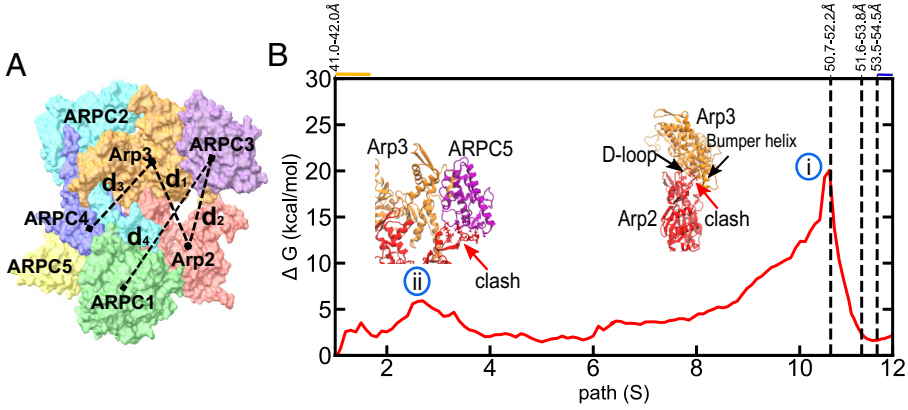

Fig. 2. Arp2/3 complex crosses an energy barrier of 20 ± 6 kcal/mol between the inactive state and the active state in the branch junction. (*A*) A linear combination of four distances d_1 to d_4 was used to define the path for pathCV-based free energy sampling (Eqs. **1** and **2**). The distances are d_1 between centers of mass of SD3 and SD4 of Arp2 and Arp3, d_2 between centers of mass of Arp2 and ARPC3, d_3 between centers of mass of Arp3 and ARPC4 and d_4 between ARPC1 and ARPC3. (*B*) Free energy profile of Arp2/3 complex along the pathway to branch formation obtained by averaging PMF from metadynamics, umbrella and equilibrium MD simulations along the reweighted pathCV from the active to the inactive states. On the *Bottom* *x*-axis, a CV value of 1 corresponds to the active, short-pitch state and 12 corresponds to inactive, splayed state, while 2 to 11 are intermediate states. The numbers on the *Top* *x*-axis give the distributions of distances d_1 of the active (41.0 to 42.0 Å), transition (50.7 to 52.2 Å), partially active (51.6 to 53.8 Å), and inactive (53.5 to 54.5 Å) states. The inactive and active states are separated by (i) a major barrier of 20 ± 6 kcal/mol (mean ± SD) and (ii) a minor free energy barrier of ~6 ± 0.7 kcal/mol. Ribbon diagrams show clashes of the D-loop of Arp2 with (i) the bumper helix of Arp3 and (ii) ARPC3. Bars just above the X-axis indicate the parts of the profile used to measure the free energies of the active, short-pitch conformation (orange) and the inactive, splayed conformation (blue).

Due to the linear nature of this transformation, the forward and reverse paths generate the same structures. The path collective variable was then defined based on the distances d_1 to d_4 that correspond to the distances between the centers of mass of the subunits that were selected based on their maximum difference between the two states (Fig. 2*A*). Biasing all four distances ensures that not just the Arps, but all the subunits move during the conformational transition. Path collective variable (32) is given by

$$S = \frac{\sum_{i=1}^{N} i\exp(-\lambda R[X - X_i])}{\sum_{i=1}^{N} \exp(-\lambda R[X - X_i])}, \quad [1]$$

where X represents the coordinates of the current simulation step and X_i is the i-th frame on the path. The function R is the metric that is a combination of distances d_1 to d_4 where the distances are weighted equally:

$$R[X - X_i] = \sum_{j=1}^{4} (d_j - d_{i,j})^2. \quad [2]$$

Metadynamics simulations showed a large and relatively sharp free energy barrier of ~27 kcal/mol (*SI Appendix*, Fig. S2*A*) as the D-loop of Arp2 moved past the bumper helix of Arp3. For additional sampling in this high free energy region, umbrella sampling simulations were performed in the pathCV region between 6.5 and 11. Umbrella sampling simulations use a harmonic bias in adjacent windows to sample conformations obtained from the metadynamics simulations along the pathCV. The free energy along the path is estimated by reweighting the sampled distribution. The high energy barrier was maintained but reduced by the umbrella sampling (*SI Appendix*, Fig. S2*A*). Fig. 2*B* plots the averaged potential of mean force (PMF) from the metadynamics and US simulations. The free energy for the region between pathCV values of 11 to 12 was calculated from the conformations sampled in the 2.2 μs long equilibrium simulation of free, inactive Arp2/3 complex (pdb id: 4JD2) (*SI Appendix*, Fig. S2*B*).

The free energy calculations revealed two barriers between the inactive and active states of Arp2/3 complex (Fig. 2*B*). The higher free energy barrier [marked (i) in Fig. 2*B*] of ~20 kcal/mol corresponds to the conformation where the D-loop of Arp2 collides with the bumper-helix of Arp3 (residues 348K-353L) (Fig. 2*B*) as observed in steered MD simulations (33). In this conformation, the distance between the centers of mass of SD3 and SD4 of Arp2 and Arp3 is 50.7 to 52.2 Å, close to the distance of 50.4 Å observed in the cryo-EM structure of the transition state of bovine Arp2/3 complex (pdb id: 7T5Q). Umbrella sampling simulation of the transition to the short-pitch state revealed a standard deviation of 6 kcal/mol in the energy barrier due to fluctuations in the conformations of the D-loop of Arp2 and the bumper helix of Arp3. Collisions between the D-loop and bumper helix result in high free energy barriers. Lower free energy barriers correspond to conformations with the D-loop separated from the bumper helix, which allow Arp2 to move past the bumper helix (*SI Appendix*, Fig. S3).

Arp2/3 complex must pass a second free energy barrier of about 6 kcal/mol to reach the active, short-pitch state (Fig. 2*B*). This barrier is due to a collision of the D-loop of Arp2 with ARPC3 (Fig. 2*B*). This free energy barrier is smaller than the first; the flexibility ARPC3 observed by their root mean squared fluctuation in *SI Appendix*, Fig. S8*E* may allow it to move away in response to the collision.

Rate and Equilibrium Constants for the Equilibrium between the Splayed and Short-Pitch States. We used the free energy data in Fig. 2*B* to estimate the rate and equilibrium constants for the interchange between the splayed and short-pitch conformations of Arp2/3 complex (Fig. 1) as well as the rate constant for crosslinking Arp2 and Arp3. The free energy of the short-pitch conformation is ~3 kcal/mol from free energy between path(S) CV values of 1 and 2. The free energy of the splayed conformation is ~1 kcal/mol from the free energy between path.S values of 11.75 and 12. Thus, $\Delta G°$ is ~2 to 3 kcal/mol and $K = \exp(-\Delta G°/RT)$ gives an equilibrium constant $K_{1\text{-}2}$ in the range 0.006 to 0.03.

Using Erying transition state theory with a transmission coefficient of unity and an average barrier of 20.5 kcal/mol we calculate the rate constant to cross the barrier k_{+1} is ~0.006 s^{-1}. From $K_{1\text{-}2} = k_{+1}/k_{-1}$, unknown k_{-1} ranges from 1 to 5 s^{-1}. Alternatively, k_{-1} can be estimated independently from the free energy profile. Free energy of activation from short-pitch to splayed conformation is around 16.5 to 17.5 kcal/mol which also results in a rate constant k_{-1} between 1 s^{-1} and 5 s^{-1}. Therefore, at 310 K Arp2/3 complex has a free energy high enough to visit the short-pitch conformation spontaneously about every 2 min.

With these parameters, we estimated the unknown rate constant for crosslinking Arp2 and Arp3 in bulk samples of Arp2/3 complex (21, 25). We assumed only the short-pitch species can be crosslinked. From $K_{1\text{-}2}$ the fraction of Arp2/3 complex in the short-pitch conformation at equilibrium is between 0.006 and 0.03, so the crosslinking rate constant ranges between 0.007 s^{-1} and 0.033 s^{-1} to give the observed rate of accumulation of crosslinked products of 0.0002 s^{-1} (24). The half times for crosslinking are between 21 s and 100 s, so most Arp2/3 complex cycles back and forth between the splayed and short-pitched conformations a few times before being irreversibly trapped in the short-pitch conformation by crosslinking.

Systems Studied by All-Atom Molecular Dynamics Simulations. To study the roles of the N-WASP-CA motif and an actin monomer in activation of Arp2/3 complex, we ran unbiased all-atom MD simulations of Arp2/3 complex starting with four different structures: i) The cryo-EM structure of human Arp2/3 complex bound to two copies of *Mus musculus* N-WASP-CA [pdb id: 6UHC (24)]; ii) a cryo-EM structure of inactive *Bos taurus* Arp2/3 complex [pdb id: 4JD2 (34)]; iii) a cryo-EM structure of *B. taurus* Arp2/3 complex bound to an actin monomer and the N-WASP CA motif fused to the α and β subunits of the CapZ [pdb id: 7T5Q (35)], which is interpreted to be a transition state, after removing the CapZ-CA fusion protein; and iv) the 7T5Q structure after removing both the CapZ-CA fusion protein and actin monomer. *SI Appendix*, Table S1 contains a summary of distances between the Arps, Arp dihedral angles, and clamp dihedral angles in the starting structures and after simulations.

Contacts between the C Helix and Distal A Region of CA with Inactive Arp2/3 Complex Persist in Atomistic MD Simulations. We ran simulations of human Arp2/3 complex bound to two copies of *M. musculus* N-WASP-CA to a) refine the structure based on the cryo-EM reconstruction [pdb id: 6UHC (24)], b) characterize the dynamics of the interactions, and c) investigate why Arp2/3 complex was in the inactive conformation despite biochemical evidence that Arp2/3 complex is more likely to visit the short-pitch conformation with bound CA (Fig. 3). The cryo-EM map has densities for both C-helices and C-terminal EWE motifs but not A motif residues 478 to 496 bound to Arp3 or residues 479 to 497 bound to Arp2/ARPC1. This highly mobile linker is enriched in negatively charged aspartic and glutamic acid residues (D/E loop). *SI Appendix*, Figs. S4 and S5 and section 3 provides a detailed description of the contacts formed between the C helix and the C-terminal of A motif with Arp2/3 complex.

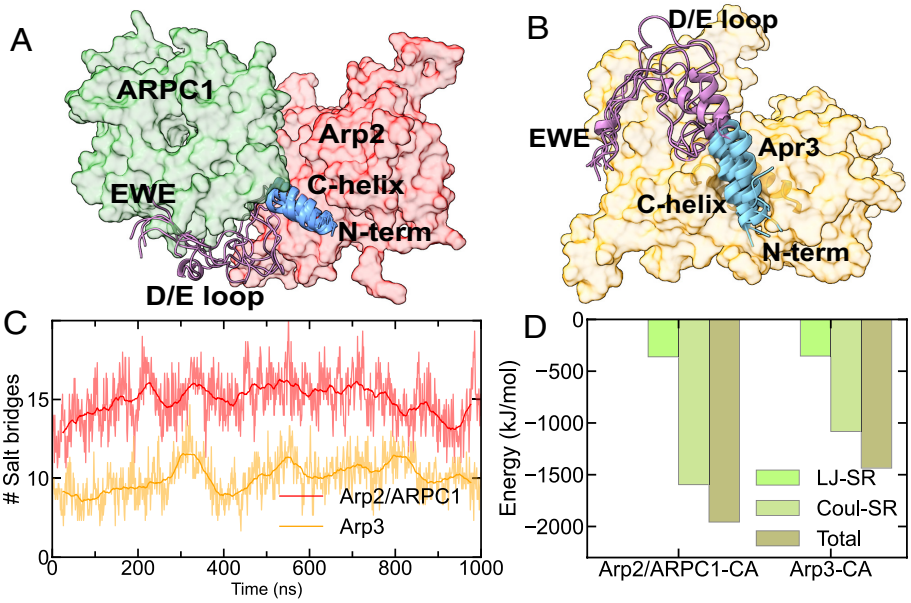

Fig. 3. MD simulations over 3.4 μs of two copies of human N-WASP CA bound to inactive human Arp2/3 complex starting with the cryo-EM structure pdb 6UHC (24). (*A* and *B*) Space-filling models of subunits of Arp2/3 complex with ribbon diagrams of the CA motifs (*C* in cyan and *A* in magenta) rendered every 560 ns. (*A*) Arp2 (red) and ARPC1 (green). (*B*) Arp3 (orange). Contacts of C helix (cyan) with Arp2 and Arp3 and the EWE motif with ARPC1 and Arp3 are relatively stable, but the D/E loops of the A motifs (magenta) adopt multiple conformations. (*C*) Numbers of salt bridges between aspartate and glutamate residues in the A motif and arginine and lysine residues in Arp2/ARPC1 and Arp3 subunits during 1 μs of MD simulation. Lighter traces are averages across three independent simulations and solid lines are their running averages with a window of 50 ns. (*D*) Lennard-Jones and Coulombic interaction energies between CA and Arp2/3 complex subunits at short range confirm that electrostatic interactions are more favorable with Arp2/ARPC1 than Arp3.

All-atom MD simulations at physiological temperature (Figs. 3, 4, and 5) revealed three important features of Arp2/3 complex with two bound CAs:

1.Conformations and interactions of D/E loops between the C-helix and the EWE motif

The MD simulations show why residues 478 to 496 in the A motif are absent from both Arp2/ARPC1 and Arp3 in the cryo-EM reconstruction; both are highly dynamic with multiple conformations and large root mean square deviations of the atoms (Fig. 3 *A* and *B* and *SI Appendix*, Fig. S6 *A* and *B*). Aspartic and glutamic acid residues in the D/E loop make salt bridges with arginine and lysine residues of Arp2, ARPC1, and Arp3 (Fig. 3*C*). However, the dynamic nature of their conformations makes these electrostatic interactions transient, and more so with Arp3 than Arp2/ARPC1 (*SI Appendix*, Fig. S6 *C–E*). The interaction energies indicate that electrostatic interactions make a larger contribution to CA binding to Arp2/ARPC1 than Arp3 (Fig. 3*D*).

2.The C helix displaces the C-terminal tail of Arp3 opening a binding site for an incoming actin subunit

The simulations produced different changes in the contacts between N-terminal end of the C helix (residues 459 to 465) with the C-terminal tails of the Arps; contacts with Arp2 in the initial structure were lost (Fig. 4*A*), while new contacts with Arp3 residues P412-S418 displaced the C-terminal tail from its initial position (red) to multiple conformations (green) (Fig. 4 *B* and *C*). The distribution of distances d_5 between the centers of mass of the C-terminal tail (M412-V416) and the W-loop (E182-Y184) of Arp3 changed from a relatively narrow peak in inactive Arp2/3 complex to a broader distribution overlapping the inactive peak (Fig. 4*B*). Although low in probability (4.3% of the 3.4 μs simulation), displacement of the C-terminal tail more than 12.0 Å allows binding of the D-loop of an incoming actin monomer (Fig. 4*D*) overcoming the autoinhibition of the transition to the active conformation (21, 24, 36–39).

3.CA binding shifts Arp2/3 complex toward a partially active state

During 3.4 μs of simulation stable interactions between the CA motif and Arp2/3 complex shift the distribution of Arp2/3 complex conformations from the inactive, splayed state captured in the cryo-EM reconstruction (pdb id: 6UHC) toward a partially active state (Fig. 5*A*). The distance between the centers of mass of subdomains 3 and 4 of Arp2 and Arp3 (d_1) (Fig. 5*A*) changed from 54.7 Å to an average of 52.7 Å, well short of 50.4 Å in the cryo-EM reconstruction of the transition state with an actin monomer bound to Arp2/3 complex (pdb id: 7T5Q) and 42.8 Å of Arp2/3 complex in the branch junction (pdb id: 7TPT). The control 3.2 μs simulation of inactive Arp2/3 complex (4JD2) without bound CA did not transition toward a partially active conformation (*SI Appendix*, Fig. S1 and section 1).

The movement of the Arp2 and Arp3 subunits involves the rotation of the upper block formed by Arp3, ARPC2, ARPC3, and ARPC5 relative to the lower block formed by Arp2, ARPC1, and the globular portion of ARPC4. The dihedral angle of the clamp [defined in Fig. 5*C* (35)] changed from −42.7° in the splayed conformation to −32.2° indicating that clamp twisting and the motion of Arp2 and Arp3 are concerted (Fig. 5*A*). Note that while the rotation along the axis of the antiparallel alpha-helices of ARPC2 and ARPC4 is necessary to reach the short-pitch conformation, the clamp dihedral angle varied widely (25° to 30°) during simulations of Arp2/3 complex with and without CA and even when Arp2/3 complex is trapped in the transition state (Fig. 6*C* and *SI Appendix*, Table S1). While the clamp rotates flexibly, nonstochastic clamp twisting is required to bring together Arp2 and Arp3 to the short-pitch conformation.

During the limited rotation toward the partially active state with bound CA, the dihedral angles formed by the four subdomains of Arp2 and Arp3 (SD2-SD1-SD3-SD4) changed small amounts (*SI Appendix*, Fig. S7). In the cryo-EM structure, the dihedral angles are −8.6° for Arp2 and −18.8° for Arp3. During the simulation, Arp2 and Arp3 subunits adopt a more twisted conformation with subunit dihedral angles of −16.1 ± 4.0° (mean ± SD) for Arp2 and −30.1 ± 4.0° for Arp3 similar to the inactive state where these dihedral angles are −19.8 ± 3.4° for Arp2 and −28 ± 3.3° for Arp3.

CA binding affects the correlated motions of Arp2/3 complex (*SI Appendix*, Fig. S8). The K-means clustering of correlated fluctuations (40) of residues indicates CA binding amplifies correlated fluctuations of the bumper helix of Arp3, D-loop of Arp2, and the protrusion helix of ARPC1. This provides hints about how CA binding enables the transition of Arp2/3 complex to the partially active state.

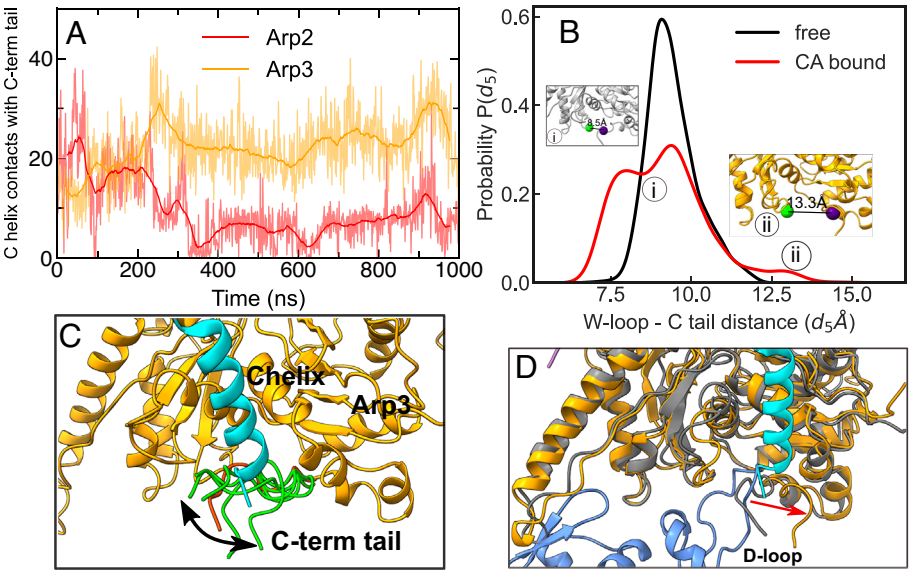

Fig. 4. Interactions of N terminus of the C helix of CA with C-terminal tail of Arp3. (*A*) Time courses of the number of steric contacts calculated to be within 4 Å between N terminus of the C-helix and C terminal tails of the Arp2 (red) and Arp3 (orange). Lighter traces are average across three independent simulations and solid lines are their running averages with a window of 50 ns. (*B*) Probability distributions of distances (d_5) between the centers of mass of the W-loop (E182-Y184) (purple spheres) and the C-terminal tail of Arp3 (P412-V416) (green); *Insets* (i) and (ii) are examples of two conformations with distances marked on the graph. (*C*) Ribbon diagrams show the C-helix (cyan) displacing the C-terminal tail of Arp3 (orange) from its starting position (red) every 560 ns during the simulation (green). (*D*) Ribbon diagrams comparing the conformations of Arp3 in the cryo-EM structure 6UHC (gray) and the end of the 3.4 μs simulation (orange). The N terminus of the C-helix (cyan) displaces the C-terminal tail of Arp3 from the barbed end groove creating space for the D-loop of an actin monomer (blue) to bind.

MD Simulations of the Transition State of Arp2/3 Complex. A structure of bovine Arp2/3 complex with a conformation intermediate between the splayed and short-pitch states was stabilized for cryo-EM by binding a CapZ heterodimer with the CA region of N-WASP fused at the C termini of the α and β subunits along with one actin monomer (PDB id: 7T5Q) (35). The cryo-EM reconstruction shows the actin subunit bound at the barbed end of Arp3, while CapZ-CA precludes actin binding to Arp2. The distance between Arp2 and Arp3 subunits is about 50 Å owing to partial rotation around the ARPC2/ARPC4 helices (35) bringing the Arps into collision near the peak of the free energy barrier (Fig. 2*B*). In the transition state the D-loop of the bound actin monomer wedges between the bumper helix and an adjacent helix of Arp3 (*SI Appendix*, Fig. S9 *A–D*). This wedge displaces the bumper helix of Arp3 from its position in the splayed conformation. Displacement of the bumper helix leaves space for the movement of Arp2 block toward the short-pitch conformation without the clashes between D-loop and bumper helix.

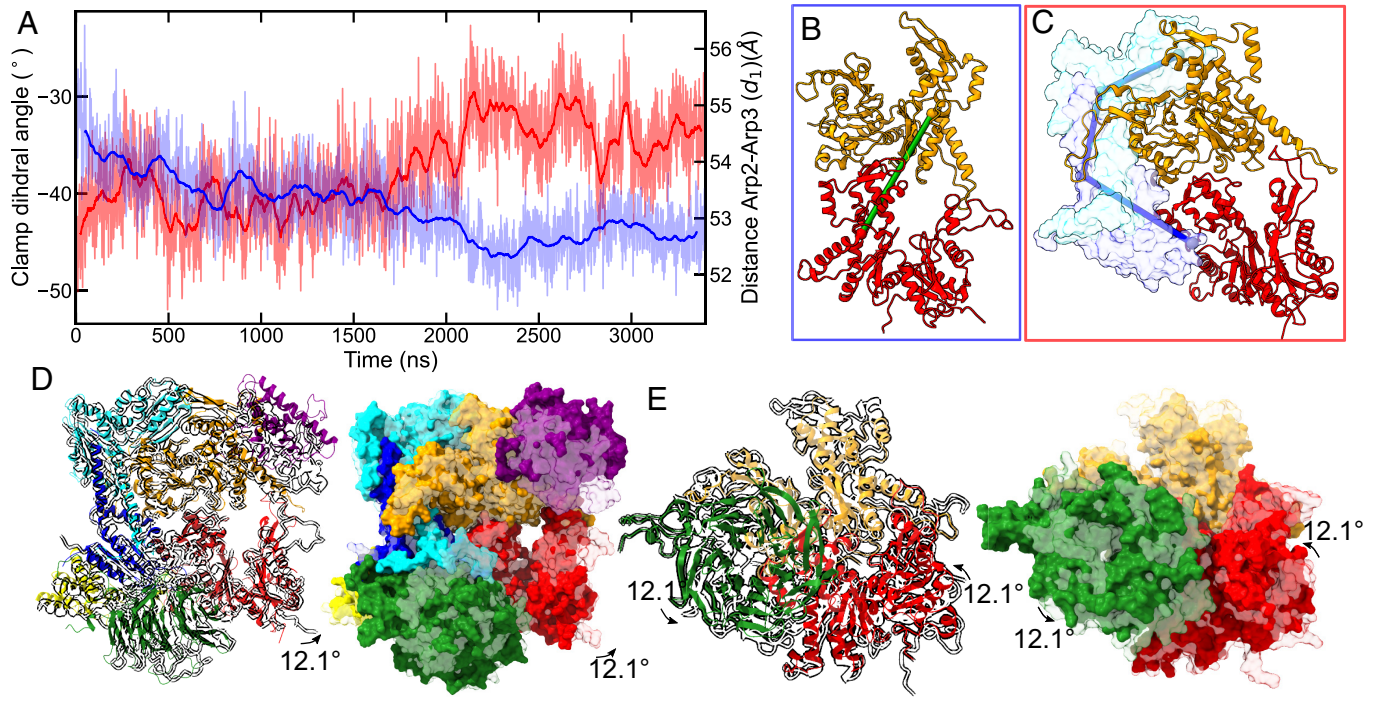

Fig. 5. The conformation of inactive, CA-bound human Arp2/3 complex (pdb id: 6UHC) shifts toward the short-pitch state during 3.4 μs of MD simulation. (*A*) During the simulation, the distance between centers of mass of subdomains 3 and 4 of Arp2 and Arp3 (blue) change from 54.7 Å to a plateau at 52.7 Å and the clamp dihedral angle (red) declines from −45.2° to −33.1°. Lighter traces are values during the simulations and solid lines are their running averages with a window of 50 ns. (*B*) Ribbon diagram with the definition of the distance between the centers of mass of subdomains 3 and 4 of Arp2 (red) and Arp3 (orange). (*C*) Ribbon diagram with the clamp dihedral angle defined by four points (centers of mass of residues K18 and I244 of ARPC2 (cyan space filling model) and R32 and S147 of ARPC4 (blue space filling model) that measures the rotation of Arp2 block relative to Arp3 block. (*D*) Conformational change in the complex during the 3.4 μs MD simulation. Ribbon diagrams of Arp2/3 complex: the outline is the starting structure; and the colored ribbon diagram is the conformation at the end of 3.4 μs. The arrow indicates the 12.1° rotation of the Arp2 block. The transparent space filling model of Arp2/3 complex is the starting structure, and the opaque space filling model is the conformation at the end of 3.4 μs. (*E*) These views down the beta-propeller of ARPC1 show ARPC1 and Arp2 rotating together toward Arp3 during the simulation.

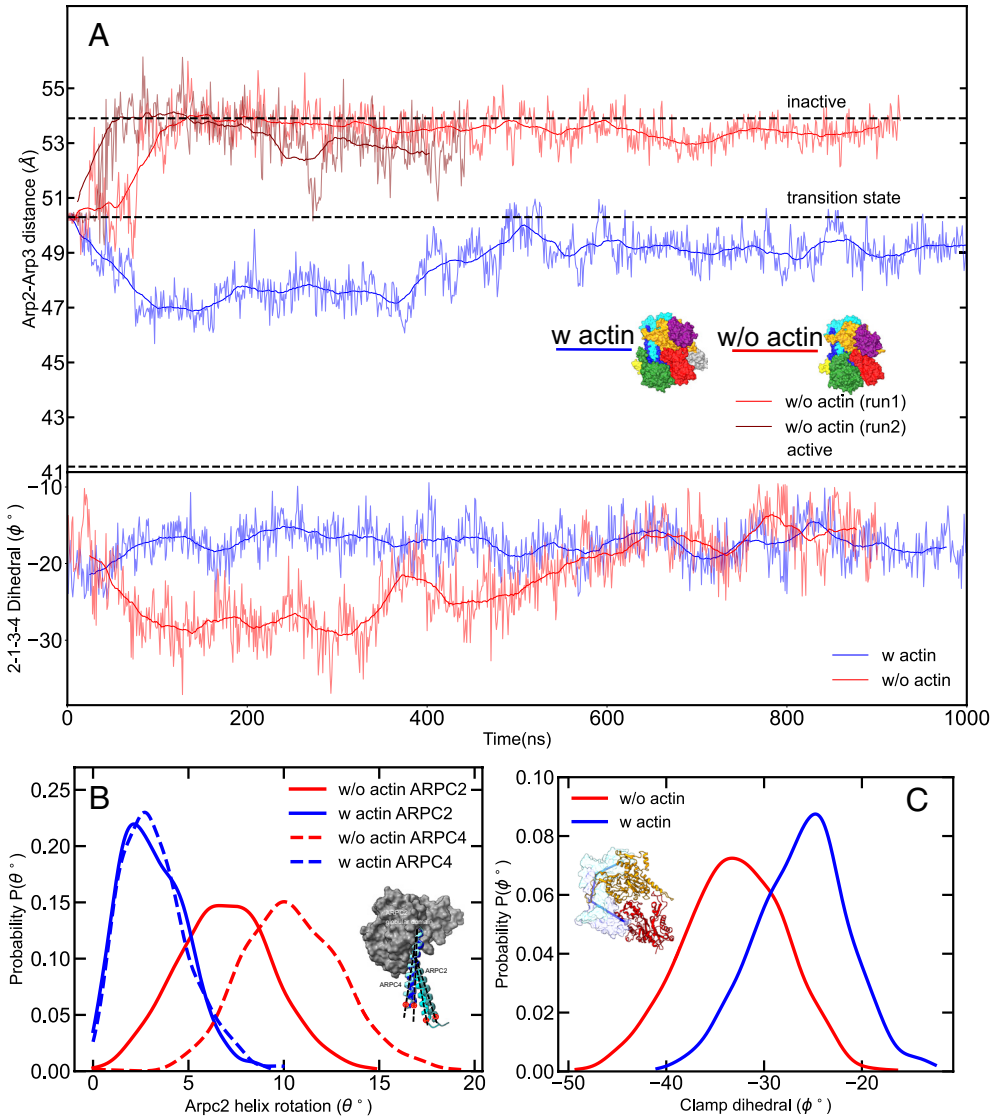

Fig. 6. MD simulations based on the transition state structure [pdb id: 7T5Q (35)] without CapZ and the two CA motifs. (*A*) (*Top*) Time courses of the distance between the centers of mass of subdomains 3 and 4 of Arp2 and Arp3 in Arp2/3 complex with (blue) and without (red) bound actin. In two replica runs without the actin monomer, Arp2/3 complex transitioned rapidly toward the distance in the splayed, inactive state (black dashed line). Space filling diagrams show the two starting structures. (*Bottom*) Time course of a transient increase in the dihedral angle of Arp3 after removing the actin monomer (red). Dihedral angle is constant when the actin monomer is bound to Arp3 (blue). (*B*) Orientations of the C-terminal helices of ARPC2 and ARPC4 changed relative to the ARPC2 globular domain before and after removing actin. Rotation of the helices is calculated by superposition of the ARPC2 globular domain (gray space filling model). The conformation of the transition state with actin is shown with lighter shades and the relaxed structure without actin at the end of the simulation is shown with darker shades. Movement of the ARPC2 helix was measured between vectors connecting the centers of mass of Y250 and A280 in both structures. Movement of the ARPC4 helix was measured between vectors connecting the centers of mass of E140 and A161 in both structures. During simulation after actin removal, the ARPC2 helix pivoted about 7.5° and the ARPC4 helix pivoted about 10°. (*C*) After removing actin, the distributions of clamp dihedral angles decreased from an average of −26.2° to −33.1°.

To characterize the effects of the actin monomer bound to the Arp2/3 complex transition state, we ran MD simulations with the CapZ-CA construct removed or both the CapZ-CA construct and actin removed (Fig. 6).

The Bound Actin Monomer Stabilizes the Transition State of Arp2/3 Complex. Remarkably, the bound actin monomer alone stabilized the transition state of Arp2/3 complex for at least a microsecond of MD simulation during which the distance between the Arp2 and Arp3 subunits was stable at 49.1 ± 0.6 Å (mean ± SD) (Fig. 6*A*), close to 50.4 Å observed in the cryo-EM structure (35). In the actin bound complex the dihedral angle of Arp3 was stable at −32.7 ± 2.8°, which is closer to the dihedral angle of −30.2° in the active state than −42.6 ± 4.0° in the inactive state.

Arp2/3 Complex Rapidly Rotates toward the Splayed State if Actin Is Removed from the Transition State. When we removed the actin monomer at the start of the simulation, the two structural blocks of Arp2/3 complex rapidly rotated from their high energy positions near the energy barrier in Fig. 2*B* toward the inactive, splayed state as indicated by changes in three parameters. First, the distance between the Arps increased ~5 Å in less than 150 ns (Fig. 6*A*). Arp3 flattened transiently (Fig. 6*A*). Second, distributions of the clamp dihedral angles between the upper block of subunits (Arp3, ARPC2, ARPC3, and ARPC5) and the lower block of subunits (Arp2, ARPC1, and the globular portion of ARPC4) decreased from an average of −26.2° to −33.1° (Fig. 6*C*). Third, the vectors between the C-terminal helices of both ARPC2 and ARPC4 changed relative to ARPC2 globular domain by 7.5° and 10° (Fig. 6*B*).

We used Hetero Elastic Network Modeling (hENM) (41) to measure the strength of interactions (effective spring constants) between the subunits of Arp2/3 complex in the transition state and after relaxing toward the splayed state after removing actin (*SI Appendix*, Fig. S9*E*). The effective attractive interactions between the Arp2 and Arp3 subunits are stronger, while the interactions between Arp2 and ARPC1, Arp3 and ARPC2, and Arp3 and ARPC3 are weaker. The changes in intersubunit interactions learned from the all-atom MD sampling can be used to develop coarse-grained interactions between subunits that enable modeling Arp2/3 complex activation and ultimately model actin filament branches.

Discussion

This work extends prior computational studies on remodeling actin filaments (11, 29, 33, 42–52) using equilibrium MD simulations and enhanced sampling at 310 K to investigate the structures and free energy along the pathway of actin filament branch formation by Arp2/3 complex. We present information on the structures and interactions of the acidic D/E loop of N-WASP CA bound to two sites on Arp2/3 complex, but this discussion focuses on insights about the pathway from free Arp2/3 complex to the initiation of the daughter filament branch on the side of the mother filament.

A wide range of experiments support a pathway of branch formation starting with free Arp2/3 complex, which first binds two copies of actin-VCA and then binds to the side of an actin filament before nucleating a daughter filament (17, 24, 53) (Fig. 7). The figure includes important structures and what is known about the kinetics and thermodynamics along the pathway.

The rate and equilibrium constants were estimated as follows: Reaction 1-3, actin-VCA binding to inactive Arp2/3 complex: The rate constants for VCA were measured directly (54). We assume that actin-VCA binds similarly. Reaction 1-2, Equilibria between splayed and short-pitch conformations of Arp2/3 complex: Rate constants and the equilibrium constant were calculated from free energy measurements (Fig. 2). Reaction 3-4, Equilibria between splayed and short-pitch conformations of Arp2/3 complex with bound actin-VCA: Rate constants are not known, but we estimate the equilibrium constant is 10-fold stronger than reaction 1-2 from the rates of crosslinking Arp2 and Arp3 (24). Reaction 2-4, Actin-VCA binding to short-pitch Arp2/3 complex: We calculated the equilibrium constant by detailed balance from the equilibrium constants for reactions 1-2, 1-3, and 3-4. The affinity of actin-VCA for short-pitch Arp2/3 complex is about 10-fold higher than the splayed conformation. Reaction 3-5, Equilibrium between splayed and transition states of Arp2/3 complex: The forward rate constant is not known, but our simulation of the transition state without actin shows that reversion to the splayed partially active state (3) is very fast, if actin dissociates. Reaction 4-5, Equilibrium between the transition and short-pitch states: This reaction has not been characterized. We assume the short-pitch state (4) is more likely to revert to the partially active state (3) than the transition state (5). Reaction 4-6, Initial binding of Arp2/3 complex to a mother filament: The measured association rate for budding yeast Arp2/3 complex is slow and dissociation is fast (20). We assume conformation of short-pitch species 4 is more favorable for binding the filament than species 5. Binding of animal and fission yeast Arp2/3 complex to actin filaments is likely to be slower than spontaneously active budding yeast Arp2/3 complex. Reaction 6-7, Conversion of Arp2/3 complex from weakly (6) to strongly bound (7) to the mother filament: This reaction was measured as the rate that bound budding yeast Arp2/3 complex initiates a daughter filament (20). VCA dissociates before the daughter filament elongates (20).

VCA motifs of NPFs, actin monomers bound to VCA, the mother filament, and the daughter filament all contribute to driving the binding reactions and conformational changes on the path to the stable, short-pitch conformation in the branch junction.

Equilibrium between Splayed and Short-Pitch Conformations. The path begins with free Arp2/3 complex in the splayed conformation (Species 1) in equilibrium with the short-pitch conformation (Species 2). Our metadynamics simulations revealed a large free energy barrier of ~20 kcal/mol between the splayed and short-pitch conformations (Fig. 2), which arises from clashes between the D-loop of Arp2 and bumper helix of Arp3. This clash was first seen in steered molecular dynamics simulations (33), where it prevented further rotation of the two blocks of structure to the short-pitch conformation in 11 of 12 simulations.

Our analysis of free energies revealed the splayed conformation is strongly favored ($K_{1\text{-}2}$ = 0.006 to 0.03), so less than 1 to 3% of Arp2/3 complex is in the short-pitch conformation. Nevertheless, Arp2 and Arp3 can be chemically crosslinked between cysteines engineered into Arp2 and Arp3 when Arp2/3 complex spontaneously visits the short-pitch conformation (21, 24, 25). While transiently in the short-pitch conformation, crosslinking is slow with a rate constant of 0.007 to 0.033 s^{-1} so crosslinked products accumulate slowly at 0.0002 s^{-1} for human Arp2/3 complex (24).

VCA Binding to Arp2/3 Complex. VCA binds to free, splayed Arp2/3 complex in a fast, diffusion-limited reaction (54) yielding species 3. Binding reverses at 10 s^{-1}, so VCA exchanges rapidly. We assume that actin-VCA binds similarly. Given the high concentrations of actin and NPF's (55) and the affinity of VCA for actin (K_d < 1 μM) (54), we expect a large fraction VCA is bound to actin either before or after binding Arp2/3 complex.

Effect of Bound VCA on Arp2/3 Complex. Species 3 (splayed, partially active Arp2/3 complex with two bound VCAs) is in equilibrium with the short-pitch species 4. Crosslinked Arps accumulate about five times faster with bound VCA and 10 times faster with bound actin-VCA (24), so both favor the short-pitch conformation. Our simulations revealed two reasons why bound CA promotes activation of Arp2/3 complex.

First, during MD simulations, the conformation of Arp2/3 complex with bound CA shifts from the initial splayed inactive conformation preserved during freezing for cryo-EM shifted toward the short-pitch conformation (Fig. 5) as originally observed by FRET (17). The Arp2/ARPC1/ARPC4 block of subunits rotates −12.1° relative to the rest of the complex. Although far from the short-pitch conformation, this "partially active" conformation may increase the visits to the short-pitch conformation, explaining how CA favors binding of Arp2/3 complex binding to filaments (18).

Readers of this paper will be interested in a paper by Saks et al. that was submitted to PNAS simultaneously with ours (56). They used classification of particles in cryoelectron micrographs to identify new conformations of bovine Arp2/3 complex in samples with N-WASP VCA. In their reconstructions with bound VCA, the C-terminus of Arp3 and the N terminus of ARPC5 are disordered as we observe. They observe five residues of the A motif continuing the C-motif α-helix bound to Arp3, which we see at some time points of our MD simulations. Further, Arp2 and ARPC5 rotate partially toward the short-pitch conformation as we observe, but in contrast to our simulations, ARPC1 and ARPC2 do not move with Arp2.

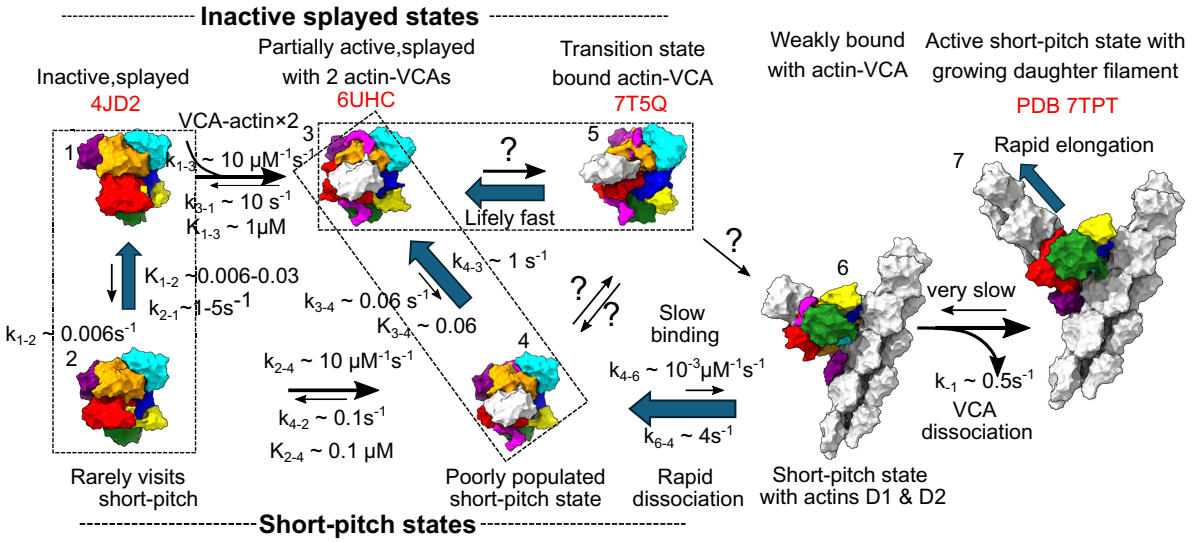

Fig. 7. Pathways from free, inactive Arp2/3 complex (1, *Upper Left*) to an actin filament branch (7, *Upper Right*). Each reactant is numbered. The dashed boxes identify reactions studied in this paper. The sizes of the arrows are proportional to measured or estimated rate or equilibrium constants for each reaction. The ratios of rate constants (k) are the equilibrium constants (K). Reactants 1 and 3 have splayed conformations. Reactants 2, 4, 6, and 7 have short-pitch conformations. Reactant 5 has an intermediate conformation. The text explains how the rate and equilibrium constants for each reaction were measured or estimated.

Second, CA binding changes the conformation of the C-terminus of Arp3 (Fig. 4). During the simulations, the N terminus of the C helix of CA displaced the C-terminal tail of Arp3 from the barbed end groove 4.3% of the time. This provides space for the D-loop of an incoming actin subunit to bind Arp3 and confirms previous work showing that the C-terminal tail of Arp3 inhibits and the C-helix promotes actin binding (36). The actin monomer bound to Arp3 promotes the short-pitch conformation judging from polymerization and crosslinking experiments (24).

CA binding also changes the internal dynamics of Arp2/3 complex. CA binding causes distributed, nonlocal effects on the dynamics of Arp2/3 complex (*SI Appendix*, Fig. S8). CA binding shifts the collective fluctuations identified by KMC-CG analysis (40) (*SI Appendix*, Fig. S8). The largest changes were enhanced fluctuations of the bumper helix of Arp3, the D-loop of Arp2, and the protrusion helix of ARPC1. These altered dynamics may facilitate the shift of Arp2/3 complex to the partially active state. These changes that occur within nanoseconds could shed light on how CA binding contributes to activating Arp2/3 complex during experiments on much slower time scales (21, 25).

Transition State. The cryo-EM structure (35) of Arp2/3 complex bound to a CapZ heterodimer with the CA motif of N-WASP fused at the C termini of the α and β subunits and carrying an actin monomer interacting with Arp3 and Arp2 (PDB id: 7T5Q) has a conformation between the splayed and short-pitch states. The structure places it on the inactive side of the major energy barrier (Fig. 2*B*), so we place this high energy state in the upper row in Fig. 7 with other splayed structures. Our MD simulation starting with this fascinating transition state revealed 3 insights.

First, the actin monomer bound to Arp3 stabilizes the transition state. We were surprised that the transition state was stable for at least 1 μs after we removed the CapZ heterodimer with the CA region of N-WASP fused at the C termini of the α and β subunits, leaving behind a single actin bound to the barbed end of Arp3 and laterally to Arp2 (Fig. 6*A*). The lateral interactions with Arp2 differ from those in the branch junction, because the complex is far from the short-pitch conformation. The actin monomer bridges the D-loop of Arp2 and the bumper helix of Arp3, stabilizing the high energy transition state (*SI Appendix*, Fig. S8). This explains previous evidence (24) that actin monomers are important for CA to activate Arp2/3 complex. We expect that the lone actin monomer dissociates on time scales longer than 1 μs, so this state is likely to be unstable without CapZ fused to CA.

Second, upon removal of the actin monomer bound to the transition state, Arp2/3 complex reverted back toward the splayed state in less than 0.15 μs in two simulations (Fig. 6*A*). Thus, the natural transition state with two CA motifs delivering two actins to the barbed ends of Arp2 and Arp3 is likely to be unstable, interchanging between the splayed state 3 and short-pitch state 4.

Third, the transition state differs in both conformation and dynamics from active Arp2/3 complex in the branch junction. When extracted from a structure of the branch junction, active complex remained in the short-pitch conformation during 1 μs of all-atom MD simulation (29) having crossed the free energy barrier associated with the transition from the splayed to the short-pitch conformation (Fig. 2). Our hENM analysis shows that an actin monomer bound to Arp2/3 complex perturbs interactions between Arp2 and Arp3 and between other subunits (*SI Appendix*, Fig. S9*E*).

Binding Arp2/3 Complex to the Mother Filament. Single molecule microscopy revealed that budding yeast Arp2/3 complex binds slowly to the sides of actin filaments and the residence time is only one or a few seconds (20, 21). VCA and actin increase both the rate of binding and the low probability that Arp2/3 complex on the side of a filament producing a branch (Fig. 7). The species binding to the mother filament in these experiments to form the weakly bound collision complex is not known.

Crosslinking experiments showed that the short-pitch conformation strongly favors binding to mother filaments; actin filaments alone do not stimulate crosslinking (22), but crosslinked, short-pitch Arp2/3 complex nucleates branched actin filaments without the aid of VCA. Species 4, actin-VCA-Arp2/3 complex in the short-pitch conformation has a binding interface complementary to the surface of the mother filament. However, the concentration of Species 3, actin-VCA-Arp2/3 complex in the partially active conformation is likely to be more than an order of magnitude higher. The interface of the partially active state with actin buries a surface area of 1,900 Å^2, less than 3,500 Å^2 in the branch junction but more than the 1,700 Å^2 buried by splayed

species 1 (*SI Appendix*, Fig. S10). The concentration of transition state is unknown but is unlikely to be high. Based on these considerations, Fig. 7 shows species 4 binding reversibly to the mother filament, but species 3 and 5 may also contribute.

Maturation of the Branch Junction and Daughter Filament Formation. Additional reactions stabilize Arp2/3 complex in the branch junction. Energy for these conformational changes comes from the large surface area buried on the mother filament (3,500 Å^2), on the daughter filament (3,000 Å^2) and internally (2,300 Å^2) in the branch junction (9, 10). VCA dissociation from Arp2 and Arp3 allows binding of daughter filament subunits 1 and 2 to the Arps properly aligned in a short-pitch helix.

Pathway of Branch Formation. NPFs and actin filaments may work together in a concerted mechanism that drives the entire pathway of branch formation, or they may regulate different steps as suggested by crosslinking experiments (25) and the molecular dynamics simulations in this paper (Fig. 7). Our free energy calculations show that a barrier of ~20 kcal/mol and an equilibrium constant of 0.006 to 0.030 separate the splayed and short pitch conformations and account for the slow rate of crosslinking of the Arps. Our observations show that CA binding pushes Arp2/3 complex part way toward the short-pitch conformation and opens a binding site for actin on Arp3.

Our data support a multistep mechanism where NPFs increase the probability of rare spontaneous fluctuations that pass the large energy barrier between the splayed and short-pitch conformations, which can be stabilized by chemical crosslinking or binding to the side of an actin filament. The pathway is not linear. Rather Species 1, 2, 3, and 4 are in equilibrium. Arp2/3 complex, most likely species 4, can exit this four-way equilibrium by binding to a mother filament, dissociating CA and undergoing additional stabilizing conformational changes that allow growth of the daughter filament.

Methods

Molecular Dynamics Simulations. To characterize the interactions of NPFs and monomeric actin with the Arp2/3 complex, we performed all-atom molecular dynamics (AA MD) simulations starting from the cryo-EM structures 4JD2 (34), 6UHC (24), and 7T5Q (35). Details of the starting structure are given in the Systems Studied section and *SI Appendix*, Table S1.

To prepare for the simulation of inactive Arp2/3 complex with two bound CA's [pdb id: 6UHC (24)], we used Charmm-GUI to model as loops the missing 38 linker residues and missing residues of Arp2 and Arp3: C-terminal residues V416-S418 of Arp3; L389-R394 of Arp2; and the D-loops of Arp2 and Arp3. ATP is bound in the nucleotide binding sites of Arp2 and Arp3. The NMR structure of autoinhibited WASP core (57) was used to make an initial approximate fit of the hydrophobic side chains of the amphipathic C motif helix into the density in the cryo-EM map at the interfaces with the Arps. In the cryo-EM structure, C-helix residues I463, L467, V470, and M471 contact different residues on the Arps. The contacted residues on Arp2 were Y147 on the hinge helix, G150 and L151 on the loop following the hinge helix, and L361, I364, and M365 on the helix adjacent to the hinge helix. On Arp3 the contacted residues were A150, A151, W153 on the hinge helix and residues F379, M383, L384, T387 on the helix adjacent to hinge helix and F414 at the C-terminal tail.

These proteins were solvated in explicit TIP3P water molecules with a minimum distance of 15 Å between the protein and the box defined by periodic boundary conditions. The protein was maintained in a charge neutral condition in 0.15 M KCl salt at neutral pH. The approximate system size of the CA bound Arp2/3 system was 370,000 atoms and the transition state actin bound system is 430,000 atoms. Three replica runs were performed for the CA bound system and two replicas for the transition state complex without actin.

The AA MD simulations were carried out using Gromacs version 2021.5 (58). The Charmm36m force field with CMAP correction was used (59). Electrostatics were treated using the particle mesh Ewald sum method with a cut-off of 12 Å. A cutoff distance of 12 Å was used for the nonbonded interactions. Bond lengths involving hydrogens were constrained using the LINCS algorithm (60). Each of the system and the replica runs were first energy minimized with harmonic restrains of 400 kJ/mol on the backbone atoms and 40 kJ/mol on the side chain atoms and LINCS constraints on the H-bonds. Following the energy minimization, the restrains on the backbone and side chain atoms were sequentially removed while the protein equilibrated to the set temperature of 310 K and pressure of 1 bar. Equilibration was done in 4 steps (with harmonic force constant constraints of k = 400, 100, 40, and 10 kJ/mol/nm^2) for 25 ns in the constant NVT ensemble using the Berendsen thermostat and integration timestep of 1 fs for the initial 12 ns and 2 fs for the subsequent simulation. The restrains on the side chain atoms were slowly released followed by the backbone atoms. Following the restrained equilibration, the protein-water simulation was run for 12 ns in the constant NPT ensemble using a Nose–Hoover thermostat with a 1.0 ps coupling time constant and Berendsen barostat (61) with a 5.0 ps coupling time constant. The simulation was then continued in three replicates at constant NPT for 1 μs of production run with a 2 fs timestep. Pressure in the production was regulated using the Parrinello–Rahman barostat (62) with a coupling constant of 5.0 ps.

Enhanced Sampling Using Metadynamics on Path Collective Variables. Large conformational changes in multidomain proteins are challenging to simulate with traditional collective variable-driven well-tempered metadynamics. The large-scale conformational differences between the crystal structures of the active and inactive Arp2/3 suggest that the transition between these states involves many degrees of freedom. Hence, a single CV like distance or torsional angle might be insufficient to capture the transition and calculate the associated free energy. To describe the conformational transition between the inactive and active Arp2/3 complex, two path collective variables, $s(R)$ and $z(R)$ were defined. The variable $s(R)$ describes the progress along a reference path and $z(R)$ the distance from the reference path (30, 31). Path variable driven metadynamics simulations have been successfully employed to reconstruct the free energy landscape that agrees with experiments and other enhanced sampling methods (63–66).

The path was defined as the combination of four distances labeled as d_1 to d_4 in Fig. 2*A*. The four distances are weighted equally. Here, d_1 is the distance between center of mass of SD3 and SD4 of Arp2 and Arp3, d_2 is the distance between center of mass of Arp2 and ARPC3, d_3 is the distance between center of mass of Arp3 and ARPC4 and d_4 is the distance between ARPC1 and ARPC3. The CVs are defined as

$$s = \frac{\sum_{j=1}^{N} j \ \exp\left(-\lambda R\left[X - X_j\right]\right)}{\sum_{j=1}^{N} \exp\left(-\lambda R\left[X - X_j\right]\right)}, \quad [3]$$

$$z = -\frac{1}{\lambda} \ln\left(\sum_{j=1}^{N} \exp\left(-\lambda R\left[X - X_j\right]\right)\right), \quad [4]$$

where N is the number of intermediate frames from the inactive to active state, $R[X - X_j]$ is the distance between the instantaneous configuration and frame along the reference path obtained upon alignment in the distance CV subspace, and λ is the parameter that controls the smooth variation of s.

The reference path from partially active to active state states is defined as a linear interpolation between these two states. Ten intermediate structures were generated between the active and partially active states. The height of Gaussian bias was set to 0.24 kcal/mol and a biasing potential was added every 5000MD steps. The biasing factor was set to 100 in the limit of regular metadynamics simulation. Aggressive biasing was used to ensure that the system sampled the complete range of path.S values in computationally feasible time. The CV space sampled during the simulation and the hill heights is shown in *SI Appendix*, Fig. S2 *C–E*. λ value set to 28 nm^{-2} ensures smooth transition of path.S. The PMF calculation converged within 240 ns of metadynamics simulation (*SI Appendix*, Fig. S2*F*). The large energy barrier close to the inactive state made sampling from the inactive state difficult. Several MD runs stalled in the partially active state. Since we perform a one-dimensional sampling on the path defined by intermediates obtained from linearly morphing between the active and partially active states the PMF measured by sampling from the inactive to active state would theoretically be similar to the PMF obtained by sampling from active to

inactive state (67–69). Since the initial path obtained by linear morphing could be unphysical, conformations within 20 $Å^2$ from the initial path were allowed to be sampled during the enhanced sampling simulation. While still restrictive, it allows for sampling of conformations other than the initial estimate. All distances d_1-d_4 sample the transition from active to inactive state, thus ensuring that all subunits are moving during the conformational transition (*SI Appendix*, Fig. S2 *G–J*).

The free energy landscape generated was verified by running equilibrium MD simulations from the higher and lower free energy conformations. The higher free energy conformations transition to the lower free energy states within 2 ns of simulation whereas the lower free energy conformation fluctuates around the equilibrium (*SI Appendix*, Fig. S2 *K–M*).

The region between 6.5 and 11 path.S umbrella sampling simulations were performed to better sample the large free energy barrier region (*SI Appendix*, Fig. S2*A*). Windows were placed at an interval of 0.25 units along the path and the conformations at each window were obtained from the metadynamics simulation. A harmonic bias with spring constant of 100 kJ/mol/nm^2 was used for all the windows except the window at 10.5 and 10.75 which was set to 300 kJ/mol/nm^2 to obtain better sampling at these windows. Each window was sampled for 30 ns and the umbrella sampling simulations were combined using the Weighted Histogram Analysis Method code (70).

The free energy of the region between 11 and 12 path.S was obtained from the probability distribution of the 2.2 μs equilibrium MD simulation of free, inactive Arp2/3 complex (pdb id: 4JD2) (*SI Appendix*, Fig. S2*B*).

Analysis. The distance and dihedral angle of Arp2 and Arp3 subunits was calculated based on the definition of the Arps into four subunits. Subunits of Arp2 is defined as SD1 1–33 74–149 and 352–388, SD2 34–73, SD3 150–184 273–351, and SD4 185–272 and subdomains of Arp3 is defined as SD1 1–31 78–148 375–416, SD2: 32–77, SD3 149–197 281–374, and SD4 198–280. The position of center of mass of the Cα atoms of each subdomain was used to compute the dihedral angle SD2–SD1–SD3–SD4. The distance between Arp2 and Arp3 subunits is calculated between the center of mass of heavy atoms of inner subdomains (SD3 and SD4) of Arp2 and Arp3.

The short-range Lennard–Jones and Coulombic interaction energies of CA domain with Arp3 and Arp2/ARPC1 was calculated using the rerun function in Gromacs. The reported values were averaged across three replica simulations of CA bound Arp2/3 each of 1 μs.

We used Hetero Elastic Network Modeling (hENM) (41) and the K-Means Clustering Coarse-graining (KMC-CG) (40) analysis to evaluate how the local small-scale fluctuation changes in Arp3 upon CA binding affect global dynamics of Arp2/3 complex with bound CA. For hENM analysis, each of the Arp2/3 complex subunit was defined as a coarse-grain site and effective interactions were calculated within a cut-off of 60 Å. Average and SD were calculated by mapping the trajectory into six pieces of equal length. The first piece was excluded as relaxation.

Correlated motion analysis using KMC-CG, which can capture both the spatial and the dynamic features of Arp2/3 complex, was applied to the CA-bound system to build the CG model with an approximate resolution of 15 AA per CG bead. The whole production trajectory of the CA-bound system was used to generate the CG model. Then, the mapped AA trajectories were obtained for both CA-bound and no-CA systems by locating the CG site at the center-of-mass of all Cα atoms which belong to that CG site. Then, the mapped AA trajectory was cut into six pieces of equal length. The first piece was excluded as relaxation. The RMSF was calculated independently for each piece of trajectory, and the SD error was calculated using the last five trajectories for each system.

Data, Materials, and Software Availability. Scripts and free energy files data have been deposited in repositories https://github.com/sahithya34/-PNEST_files.git (71) and https://github.com/sahithya34/AnalysisScriptsArp2-3.git (72) (10.5281/zenodo.14607075 (73) and 10.5281/zenodo.14607081 (74)). Some study data are available; however, due to the large file sizes of the trajectories and the numerous files, the trajectories will be made available upon request.

ACKNOWLEDGMENTS. Research reported in this publication was supported by the National Institute of General Medical Sciences of the NIH under award numbers R01GM063796 to G.A.V. and R01GM026132 to T.D.P. The content is solely the responsibility of the authors and does not necessarily represent the official views of the NIH. Computational resources were provided by the University of Chicago Research Computing Center and the NIH-funded Beagle-3 computer (NIH award 1S10OD028655-01).

Author affiliations: [a]Department of Chemistry, Chicago Center for Theoretical Chemistry, Institute for Biophysical Dynamics, and James Franck Institute, The University of Chicago, Chicago, IL 60637; [b]Department of Molecular Cellular and Developmental Biology, Yale University, New Haven, CT 06511; [c]Department of Molecular Biophysics and Biochemistry, Yale University, New Haven, CT 06511; and [d]Department of Cell Biology, Yale University, New Haven, CT 06511

1. T. D. Pollard, Actin and actin-binding proteins. *Cold Spring Harb. Perspect. Biol.* **8**, a018226 (2016).
2. L. G. Tilney, M. S. Tilney, Observations on how actin filaments become organized in cells. *J. Cell Biol.* **99**, 76s–82s (1984).
3. L. M. Machesky, S. J. Atkinson, C. Ampe, J. Vandekerckhove, T. D. Pollard, Purification of a cortical complex containing two unconventional actins from Acanthamoeba by affinity chromatography on profilin-agarose. *J. Cell Biol.* **127**, 107–115 (1994).
4. R. D. Mullins, J. A. Heuser, T. D. Pollard, The interaction of Arp2/3 complex with actin: Nucleation, high affinity pointed end capping, and formation of branching networks of filaments. *Proc. Natl. Acad. Sci. U.S.A.* **95**, 6181–6186 (1998).
5. R. D. Mullins, W. F. Stafford, T. D. Pollard, Structure, subunit topology, and actin-binding activity of the Arp2/3 complex from Acanthamoeba. *J. Cell Biol.* **136**, 331–343 (1997).
6. L. Blanchoin *et al.*, Direct observation of dendritic actin filament networks nucleated by Arp2/3 complex and WASP/Scar proteins. *Nature* **404**, 1007–1011 (2000).
7. R. C. Robinson *et al.*, Crystal structure of Arp2/3 complex. *Science* **294**, 1679–1684 (2001).
8. F. Fäßler, G. Dimchev, V. V. Hodirnau, W. Wan, F. K. M. Schur, Cryo-electron tomography structure of Arp2/3 complex in cells reveals new insights into the branch junction. *Nat. Commun.* **11**, 6437 (2020).
9. B. Ding *et al.*, Structure of Arp2/3 complex at a branched actin filament junction resolved by single-particle cryo-electron microscopy. *Proc. Natl. Acad. Sci. U.S.A.* **119**, e2202723119 (2022).
10. S. Z. Chou, M. Chatterjee, T. D. Pollard, Mechanism of actin filament branch formation by Arp2/3 complex revealed by a high-resolution cryo-EM structure of the branch junction. *Proc. Natl. Acad. Sci. U.S.A.* **119**, e2206722119 (2022).
11. J. Pfaendtner *et al.*, Key structural features of the actin filament Arp2/3 complex branch junction revealed by molecular simulation. *J. Mol. Biol.* **416**, 148–161 (2012).
12. S. S. Chavali *et al.*, Cryo-EM structures reveal how phosphate release from Arp3 weakens actin filament branches formed by Arp2/3 complex. *Nat. Commun.* **15**, 2059 (2024).
13. A. R. Wagner, Q. Luan, S. L. Liu, B. J. Nolen, Dip1 defines a class of Arp2/3 complex activators that function without preformed actin filaments. *Curr. Biol.* **23**, 1990–1998 (2013).
14. E. D. Goley, S. E. Rodenbusch, A. C. Martin, M. D. Welch, Critical conformational changes in the Arp2/3 complex are induced by nucleotide and nucleation promoting factor. *Mol. Cell* **16**, 269–279 (2004).
15. R. Rohatgi *et al.*, The interaction between N-WASP and the Arp2/3 complex links Cdc42-dependent signals to actin assembly. *Cell* **97**, 221–231 (1999).
16. H. N. Higgs, L. Blanchoin, T. D. Pollard, Influence of the C terminus of Wiskott-Aldrich syndrome protein (WASp) and the Arp2/3 complex on actin polymerization. *Biochemistry* **38**, 15212–15222 (1999).
17. S. Espinoza-Sanchez, L. A. Metskas, S. Z. Chou, E. Rhoades, T. D. Pollard, Conformational changes in Arp2/3 complex induced by ATP, WASp-VCA, and actin filaments. *Proc. Natl. Acad. Sci. U.S.A.* **115**, E8642–E8651 (2018).
18. S. C. Ti, C. T. Jurgenson, B. J. Nolen, T. D. Pollard, Structural and biochemical characterization of two binding sites for nucleation-promoting factor WASp-VCA on Arp2/3 complex. *Proc. Natl. Acad. Sci. U.S.A.* **108**, E463–E471 (2011).
19. L. M. Machesky *et al.*, Scar, a WASp-related protein, activates nucleation of actin filaments by the Arp2/3 complex. *Proc. Natl. Acad. Sci. U.S.A.* **96**, 3739–3744 (1999).
20. B. A. Smith, K. Daugherty-Clarke, B. L. Goode, J. Gelles, Pathway of actin filament branch formation by Arp2/3 complex revealed by single-molecule imaging. *Proc. Natl. Acad. Sci. U.S.A.* **110**, 1285–1290 (2013).
21. M. Rodnick-Smith, Q. Luan, S. L. Liu, B. J. Nolen, Role and structural mechanism of WASP-triggered conformational changes in branched actin filament nucleation by Arp2/3 complex. *Proc. Natl. Acad. Sci. U.S.A.* **113**, E3834–E3843 (2016).
22. A. M. Gautreau, F. E. Fregoso, G. Simanov, R. Dominguez, Nucleation, stabilization, and disassembly of branched actin networks. *Trends Cell Biol.* **32**, 421–432 (2022).
23. F. Fäßler, M. G. Javoor, F. K. Schur, Deciphering the molecular mechanisms of actin cytoskeleton regulation in cell migration using cryo-EM. *Biochem. Soc. Trans.* **51**, 87–99 (2023).
24. A. Zimmet *et al.*, Cryo-EM structure of NPF-bound human Arp2/3 complex and activation mechanism. *Sci. Adv.* **6**, eaaz7651 (2020).
25. H. Y. Narvaez-Ortiz, B. J. Nolen, Unconcerted conformational changes in Arp2/3 complex integrate multiple activating signals to assemble functional actin networks. *Curr. Biol.* **32**, 975–987.e6 (2022).
26. S. Kumar, J. M. Rosenberg, D. Bouzida, R. H. Swendsen, P. A. Kollman, The weighted histogram analysis method for free-energy calculations on biomolecules. I. The method. *J. Comput. Chem.* **13**, 1011–1021 (1992).
27. B. Roux, The calculation of the potential of mean force using computer simulations. *Comput. Phys. Commun.* **91**, 275–282 (1995).
28. G. M. Torrie, J. P. Valleau, Nonphysical sampling distributions in Monte Carlo free-energy estimation: Umbrella sampling. *J. Comput. Phys.* **23**, 187–199 (1977).
29. Y. Singh, G. M. Hocky, B. J. Nolen, Molecular dynamics simulations support a multistep pathway for activation of branched actin filament nucleation by Arp2/3 complex. *J. Biol. Chem.* **299**, 105169 (2023).
30. D. Branduardi, F. L. Gervasio, M. Parrinello, From A to B in free energy space. *J. Chem. Phys.* **126**, 054103 (2007).

31. G. Díaz Leines, B. Ensing, Path finding on high-dimensional free energy landscapes. *Phys. Rev. Lett.* **109**, 020601 (2012).
32. L. Hovan, F. Comitani, F. L. Gervasio, Defining an optimal metric for the path collective variables. *J. Chem. Theory Comput.* **15**, 25–32 (2019).
33. P. Dalhaimer, T. D. Pollard, Molecular dynamics simulations of Arp2/3 complex activation. *Biophys. J.* **99**, 2568–2576 (2010).
34. Q. Luan, B. J. Nolen, Structural basis for regulation of Arp2/3 complex by GMF. *Nat. Struct. Mol. Biol.* **20**, 1062–1068 (2013).
35. T. van Eeuwen *et al.*, Transition state of Arp2/3 complex activation by actin-bound dimeric nucleation-promoting factor. *Proc. Natl. Acad. Sci. U.S.A.* **120**, e2306165120 (2023).
36. M. Rodnick-Smith, S. L. Liu, C. J. Balzer, Q. Luan, B. J. Nolen, Identification of an ATP-controlled allosteric switch that controls actin filament nucleation by Arp2/3 complex. *Nat. Commun.* **7**, 12226 (2016).
37. F. E. Fregoso *et al.*, Molecular mechanism of Arp2/3 complex inhibition by Arpin. *Nat. Commun.* **13**, 628 (2022).
38. M. Shaaban, S. Chowdhury, B. J. Nolen, Cryo-EM reveals the transition of Arp2/3 complex from inactive to nucleation-competent state. *Nat. Struct. Mol. Biol.* **27**, 1009–1016 (2020).
39. Q. Luan, A. Zelter, M. J. MacCoss, T. N. Davis, B. J. Nolen, Identification of Wiskott-Aldrich syndrome protein (WASP) binding sites on the branched actin filament nucleator Arp2/3 complex. *Proc. Natl. Acad. Sci. U.S.A.* **115**, E1409–E1418 (2018).
40. J. Wu, W. Xue, G. A. Voth, K-Means Clustering Coarse-Graining (KMC-CG): A next generation methodology for determining optimal coarse-grained mappings of large biomolecules. *J. Chem. Theory Comput.* **19**, 8987–8997 (2023).
41. E. Lyman, J. Pfaendtner, G. A. Voth, Systematic multiscale parameterization of heterogeneous elastic network models of proteins. *Biophys. J.* **95**, 4183–4192 (2008).
42. J. Pfaendtner, E. M. De La Cruz, G. A. Voth, Actin filament remodeling by actin depolymerization factor/cofilin. *Proc. Natl. Acad. Sci. U.S.A.* **107**, 7299–7304 (2010).
43. J. Pfaendtner, G. A. Voth, Molecular dynamics simulation and coarse-grained analysis of the Arp2/3 complex. *Biophys. J.* **95**, 5324–5333 (2008).
44. F. Aydin, H. H. Katkar, G. A. Voth, Multiscale simulation of actin filaments and actin-associated proteins. *Biophys. Rev.* **10**, 1521–1535 (2018).
45. F. Aydin *et al.*, Prediction of the essential intermolecular contacts for side-binding of VASP on F-actin. *Cytoskeleton (Hoboken)* **81**, 382–392 (2024).
46. V. Zsolnay, M. L. Gardel, D. R. Kovar, G. A. Voth, Cracked actin filaments as mechanosensitive receptors. *Biophys. J.* **123**, 3283–3294 (2024), 10.1016/j.bpj.2024.06.014.
47. A. J. Harker *et al.*, Ena/VASP processive elongation is modulated by avidity on actin filaments bundled by the filopodia cross-linker fascin. *Mol. Biol. Cell* **30**, 851–862 (2019).
48. S. Zhang, D. Vavylonis, Steps of actin filament branch formation by Arp2/3 complex investigated with coarse-grained molecular dynamics. *Front. Cell Dev. Biol.* **11**, 1071977 (2023).
49. F. Aydin, N. Courtemanche, T. D. Pollard, G. A. Voth, Gating mechanisms during actin filament elongation by formins. *Elife* **7**, e37342 (2018).
50. A. C. Schramm *et al.*, Actin filament strain promotes severing and cofilin dissociation. *Biophys. J.* **112**, 2624–2633 (2017).
51. S. Laporte, A. Magistrato, Deciphering the molecular terms of Arp2/3 allosteric regulation from all-atom simulations and dynamical network theory. *J. Phys. Chem. Lett.* **12**, 5384–5389 (2021).
52. B. G. Horan, G. H. Zerze, Y. C. Kim, D. Vavylonis, J. Mittal, Computational modeling highlights the role of the disordered Formin Homology 1 domain in profilin–actin transfer. *FEBS Lett.* **592**, 1804–1816 (2018).
53. F. Ghasemi *et al.*, Regeneration of actin filament branches from the same Arp2/3 complex. *Sci. Adv.* **10**, eadj7681 (2024).
54. J. B. Marchand, D. A. Kaiser, T. D. Pollard, H. N. Higgs, Interaction of WASP/Scar proteins with actin and vertebrate Arp2/3 complex. *Nat. Cell Biol.* **3**, 76–82 (2001).
55. H. N. Higgs, T. D. Pollard, Activation by Cdc42 and PIP of Wiskott–Aldrich syndrome protein (WASp) stimulates actin nucleation by Arp2/3 complex. *J. Cell Biol.* **150**, 1311–1320 (2000).
56. A. J. Saks, K. R. Barrie, G. Rebowski, R. Dominguez, NPF binding to Arp2 is allosterically linked to the release of ArpC5's N terminal tail and conformational changes in Arp2/3 complex. *Proc. Natl. Acad. Sci. U.S.A.*, in press.
57. S. C. Panchal, D. A. Kaiser, E. Torres, T. D. Pollard, M. K. Rosen, A conserved amphipathic helix in WASP/Scar proteins is essential for activation of Arp2/3 complex. *Nat. Struct. Biol.* **10**, 591–598 (2003).
58. M. J. Abraham *et al.*, GROMACS: High performance molecular simulations through multi-level parallelism from laptops to supercomputers. *SoftwareX* **1–2**, 19–25 (2015).
59. J. Huang *et al.*, CHARMM36m: An improved force field for folded and intrinsically disordered proteins. *Nat. Methods* **14**, 71–73 (2017).
60. B. Hess, H. Bekker, H. J. C. Berendsen, J. G. E. M. Fraaije, LINCS: A linear constraint solver for molecular simulations. *J. Comput. Chem.* **18**, 1463–1472 (1997).
61. H. J. C. Berendsen, J. P. M. Postma, W. F. van Gunsteren, A. DiNola, J. R. Haak, Molecular dynamics with coupling to an external bath. *J. Chem. Phys.* **81**, 3684–3690 (1984).
62. M. Parrinello, A. Rahman, Polymorphic transitions in single crystals: A new molecular dynamics method. *J. Appl. Phys.* **52**, 7182–7190 (1981).
63. E. Formoso, V. Limongelli, M. Parrinello, Energetics and structural characterization of the large-scale functional motion of adenylate kinase. *Sci. Rep.* **5**, 8425 (2015).
64. B. Oruganti, R. Friedman, Activation of Abl1 kinase explored using well-tempered metadynamics simulations on an essential dynamics sampled path. *J. Chem. Theory Comput.* **17**, 7260–7270 (2021).
65. L. S. M. Evenseth *et al.*, Exploring conformational dynamics of the extracellular Venus flytrap domain of the GABA(B) receptor: A path-metadynamics study. *J. Chem. Inf. Model.* **60**, 2294–2303 (2020).
66. I. Kolossváry, W. Sherman, Comprehensive approach to simulating large scale conformational changes in biological systems utilizing a path collective variable and new barrier restraint. *J. Phys. Chem. B* **127**, 5214–5229 (2023).
67. M. Invernizzi, M. Parrinello, Making the best of a bad situation: A multiscale approach to free energy calculation. *J. Chem. Theory Comput.* **15**, 2187–2194 (2019).
68. M. Salvalaglio, P. Tiwary, M. Parrinello, Assessing the reliability of the dynamics reconstructed from metadynamics. *J. Chem. Theory Comput.* **10**, 1420–1425 (2014).
69. A. Barducci, M. Bonomi, M. Parrinello, Metadynamics. *Wires Comput. Mol. Sci.* **1**, 826–843 (2011).
70. A. Grossfield, WHAM: The weighted histogram analysis method. http://membrane.urmc.rochester.edu/wordpress/?page_id=126.
71. S. S. Iyer, Free energy inputs from "Molecular mechanism of Arp2/3 activation by nucleation promoting factors and actin monomer. GitHub. https://github.com/sahithya34/-PNEST_files. Deposited 6 January 2025.
72. S. S. Iyer, Analysis Scipts from "Molecular mechanism of Arp2/3 activation by nucleation promoting factors and actin monomer." GitHub. https://github.com/sahithya34/AnalysisScriptsArp2-3. Deposited 6 January 2025.
73. S. S. Iyer, Data from "Molecular mechanism of Arp2/3 activation by nucleation promoting factors and actin monomer." Zenodo. https://doi.org/10.5281/zenodo.14607075. Deposited 7 January 2025.
74. S. S. Iyer, Data from "Molecular mechanism of Arp2/3 activation by nucleation promoting factors and actin monomer." Zenodo. https://doi.org/10.5281/zenodo.14607081. Deposited 7 January 2025.